Chemical Engineering Science 303 (2025) 120953

Contents lists available at ScienceDirect

Chemical Engineering Science

journal homepage: www.elsevier.com/locate/ces

Metal-organic framework derived Co@N/C with enhanced oxygen reduction reaction in direct borohydride fuel cells

Lianke Zhang [a], Lei Zhang [a], Dandan Li [a], Haiying Qin [a,*], Hualiang Ni [a], Hongzhong Chi [a], Junjing He [a], Yan He [b]

[a] New Energy Materials Research Center, College of Materials and Environmental Engineering, Hangzhou Dianzi University, Hangzhou 310018, PR China
[b] Shanghai Synchrotron Radiation Facility, Shanghai Advanced Research Institute, Chinese Academy of Sciences, Shanghai 201203, PR China

ARTICLE INFO

Keywords:
Co@N/C
Carbothermal shock
Core-shell
Durability
Direct borohydride fuel cells

ABSTRACT

Developing efficient and durable non-precious metals catalysts is crucial for fuel cells. Herein, we synthesize nitrogen-doped carbon-encapsulated metal cobalt nanoparticles with core–shell structure (Co@N/C-Joule) catalyst by carbothermal shock (CTS) pyrolysis of ZIF-67 under argon atmosphere. The Co@N/C-Joule exhibits superior catalytic activity and stability for the oxygen reduction reaction (ORR) in alkaline electrolyte. Co@N/C-Joule demonstrates a half-wave potential of 0.84 V (*vs.* the reversible hydrogen electrode, RHE). The Co@N/C-Joule also exhibits superior stability, with only a 4 mV negative shift after 30,000 cyclic voltammetry cycles. The direct borohydride fuel cells using the Co@N/C-Joule cathode achieves a maximum power density of 389 mW cm^{-2} at 60 °C. The rapid heating and cooling rate of CTS enables the production of small-sized Co@N/C nanocatalysts with ultra-thin nitrogen-doped graphite layer coating on Co particles, thereby increasing the surface density of active sites on Co nanoparticles and Co-N sites, which leads to improved ORR performance.

1. Introduction

Fuel cells have received significant interest for their advantages such as high performance, safety and environmental friendliness (Gao et al., 2022). Platinum-based catalysts are widely adopted as cathode catalysts for fuel cells due to their excellent catalytic performance in catalyzing the oxygen reduction reaction (ORR). Nevertheless, the high cost and limited availability of platinum present significant challenges to commercialization of fuel cells (Guo et al., 2024). Therefore, the development of non-precious metal cathode catalysts with efficiency and superior durability is crucial for fuel cells technology (Fang et al., 2024).

Transition metals (Fe, Co, Cu, Mn) are considered as promising alternatives to Pt-based catalysts for the ORR due to their high catalytic activity (Kim et al., 2019; Peng et al., 2014; Zhang et al., 2020a). The durability of hybrid Fe/Fe_3C@N-doped carbon was significantly enhanced by coating it with graphene (Fe/Fe_3C@NC-Gs), resulting in only a 5 % decrease in current density after 21,600 s of operation (Zhang et al., 2020b). Similarly, the N-Fe-CNT/CNP composite catalyst exhibited superior stability and ORR activity compared to commercial Pt/C in alkaline electrolytes (Chung et al., 2013). However, Fe-based catalysts suffer from Fenton reactions, where generated hydroxyl radicals (*OH) attack the metal centers in Fe/N/C catalysts, leading to metal ion dissolution, structural degradation, and consequently, diminished activity and stability (Miao et al., 2021). While Cu-based and Mn-based catalysts offer an alternative, their catalytic activity remains inferior to that of Fe and Co, making Co a more attractive candidate for ORR (Peng et al., 2014). Han et al. synthesized 3DCo-N-C catalysts by incorporating higher Co doping with pyridine N content into carbon nanotube precursors with g-C_3N_4. The half-wave potential ($E_{1/2}$) of these catalysts was 0.812 V (*vs.* RHE) (Han et al., 2019). Dai et al. reported a new hierarchical rod-like structure of Co@N/C material (C-MOF-C2-T) obtained by pyrolysis of 3D MOF material at high temperatures (Zhang et al., 2018). The half-wave potential of these catalysts towards ORR was 0.817 V. Previous studies have demonstrated that the coordination interactions between Co and N- carbon can generate efficient active sites, such as Co-N and Co-N-C, which significantly enhance the catalytic activity in ORR (Wang et al., 2021). However, achieving Me/N/C performance comparable to platinum-based catalysts remains a significant challenge, requiring further innovation in catalyst design and synthesis methods.

Metal-organic frameworks (MOFs) have recently been recognized as

* Corresponding author.
E-mail address: hyqin@hdu.edu.cn (H. Qin).

https://doi.org/10.1016/j.ces.2024.120953
Received 10 July 2024; Received in revised form 9 November 2024; Accepted 17 November 2024
Available online 19 November 2024

effective precursors for synthesizing Me/N/C (Peng et al., 2021). Using MOFs as precursors, researchers could create highly porous carbon materials with well-dispersed metal and nitrogen sites, which are crucial for effective ORR catalysis (Ha et al., 2020; Kumar et al., 2023; Liu et al., 2022). Additionally, the inherent porosity of MOFs facilitates mass transport and provides accessible active sites, further enhancing catalytic performance. Peng et al. synthesized Co/N/C through high-temperature pyrolysis using hybrid precursors of carbon nanofibers and ZIF-67, resulting in an $E_{1/2}$ of 0.81 V (Peng et al., 2021). Regarding the preparation methods of Co/N/C catalysts, thermal decomposition of precursors, sol-gel method, and vapor deposition method are commonly employed (Li et al., 2019; Luo et al., 2020; Stracensky et al., 2023; Zhang et al., 2017). The thermal decomposition method involves heating the precursor in a tube furnace at a high temperature (>800 °C) for one or two hours. Compared to the vapor phase deposition and sol-gel methods, thermal decomposition offers the advantages of simple operation and high controllability, making it widely used for preparing Co/N/C catalysts. However, traditional tube furnace pyrolysis suffers from high energy consumption, long preparation time, and increased sample particle size due to extended cooling time. Hu et al. proposed a method known as carbothermal shock (CTS) that introduced a novel approach to nanomaterial synthesis (Yao et al., 2018). Due to its advantages, including low energy consumption, short preparation time, and rapid cooling rates (within seconds), Yao et al. have extended the application of carbothermal shock to the realm of non-precious metals, successfully synthesizing high-density and ultrasmall Co nanoparticles on two-dimensional porous carbon (Co-N-CTS), which exhibit excellent catalytic activity and stability towards ORR and oxygen evolution reaction (Shi et al., 2023). Han et al. proposed a method for the synthesis of sub-3 nm non-precious metal nanoparticles by fast pyrolysis of MOF materials via high-temperature pulsed Joule heating (Han et al., 2022). This method could achieve at least four times the metal loading compared to previous strategies that produced ultrasmall nanoparticles (NPs) but with significant sacrifices in metal content (usually less than 10 wt%). Then, They similarly synthesized catalysts by high-temperature pyrolysis of metal ligands by means of rapid CTS (~100 ms) (Li et al., 2023). The prepared catalyst demonstrated excellent bifunctional catalyst performance and stability in the oxygen reduction reaction. The superior catalytic activity of Co/N/C is probably attributed to the crucial role of in situ metal-ligand coordination and local ordering during rapid pyrolysis.

A nitrogen doped carbon supported CoO (CoO/N/C) nanocatalyst has been prepared by carbothermal shock in the air atmosphere (Li et al., 2023). The prepared CoO/N/C exhibited good durability for ORR in an alkaline medium. Embedding the active sites within a porous structure or forming a protective carbon shell is a common approach to improve the durability of catalyst (Prieto et al., 2013; Wang et al., 2016). Herein, we reported the synthesis of nitrogen-doped carbon-encapsulated metal cobalt nanoparticles with core-shell structure (Co@N/C-Joule) nanocatalysts via carbothermal shock pyrolysis of ZIF-67 in an Ar atmosphere. In the process, a nitrogen-doped carbon film is deposited on the surface of Co NPs, forming a core-shell structure. The thin carbon film protects the Co NPs, enhancing catalytic performance. A comparison was made between samples synthesized using conventional furnace pyrolysis (denoted as Co@N/C-Tube) and CTS in Ar or Air atmosphere (denoted as Co@N/C-Joule or CoO/N/C-Joule). Co@N/C-Joule exhibited a reduction in pyrolysis time by approximately 4 orders of magnitude, alongside a decrease in carbon shell thickness from 3.3 nm to 1.3 nm, and an enhancement in electrochemical performance. Direct borohydride fuel cell (DBFC) using Co@N/C-Joule as the cathode demonstrated high power density and durability compared to the DBFC using Co@N/C-Tube cathode.

2. Experimental

2.1. Synthesis of ZIF-67 precursor

The preparation process of ZIF-67 in this study was based on a method described in the published literature (Zhao et al., 2017). Solution A was prepared by dissolving 4.2 g of $Co(NO_3)_2{\cdot}6H_2O$ into 150 mL of methanol, and 5.53 g of 2-methylimidazole was dissolved into 150 mL of methanol to form solution B. Solution A was slowly added to solution B and stirred in a closed chamber for 3 h at 25 °C, and then washed three times by centrifugation with methanol. Finally, the product was dried under vacuum in an oven at 70 °C for 18 h.

2.2. Synthesis of Co@N/C catalysts

The preparation process in this study followed a method described in a previous publication (Li et al., 2023). First, 90 mg of carbon powder (BP2000) and 110 mg of ZIF-67 were mixed with 20 mL of ethanol. The mixture was then subjected to ultrasonic dispersion for 10 min. Afterward, the dispersion was sealed and stirred for 24 h. Subsequently, 30 μL of 5 wt% Nafion solution was added and stirred until it formed a viscous slurry, which was coated onto the carbon cloth. The coated carbon cloth was cut into pieces measuring 1 cm × 1.5 cm and fastened onto the carbothermal device (Kuang et al., 2024). This carbothermal device utilized an electrolytic capacitor as a transient power source to discharge through the precursor material within milliseconds. The sintering temperature was maintained at 760 °C in an Ar atmosphere. The catalyst produced through this pyrolysis process was denoted as Co@N/C-Joule. For the preparation of CoO/N/C-Joule, the coated carbon cloth underwent pyrolysis in the air atmosphere using CTS. Additionally, precursors with identical proportions were introduced into a tube furnace. The furnace was heated at a rate of 10 °C min^{-1} under an Ar atmosphere until it reached 760 °C. After holding at 760 °C for 1 h, it was cooled down. The catalyst obtained from this process was denoted Co@N/C-Tube. The schematic of preparation of Co@N/C-Joule, Co@N/C-Tube, and CoO/N/C-Joule nanocatalysts was presented in Fig. 1. The characterization of the prepared catalysts was provided in the Supporting Information.

2.3. Electrochemical characterization

The electrocatalytic performance of the catalysts for the ORR in an alkaline electrolyte was investigated using cyclic voltammetry (CV), rotating disk electrode (RDE), and rotating ring disk electrode (RRDE) techniques in a three-electrode electrochemical system. A polished glassy carbon electrodes coated with catalysts was used as working electrode. The loadings of the prepared catalysts was 283 μg cm^{-2} and the loading of 20 wt% commercial Pt/C on the working electrode was 100 μg cm^{-2}. A 0.1 M KOH solution was used as the electrolyte, and all experiments were conducted at room temperature employing an electrochemical workstation (CHI 730e) and a rotating motor (RDE710, Gamry). Unless otherwise noted, reference potentials were given relative to the reversible hydrogen electrode (RHE). Additional information was provided in the Supporting Information.

2.4. Fuel cell test

The cell performance and stability of DBFCs were evaluated using a PFX-2011 battery tester (Kikusui Electronics Corp) at operating temperatures of 30 and 60 °C. A schematic of the single direct borohydride fuel cell was shown in Fig. S1. The active electrode area was 1 cm^2, and the catalyst loading for both the anode and cathode was 5 mg cm^{-2}. The prepared catalysts was used as cathode catalyst, while $Co(OH)_2$-PPy-BP powder reported in our previous work was used as the anode catalyst (Qin et al., 2009). Catalyst slurry was prepared by mixing the catalyst powder, 5 wt% Nafion solution, and ethanol in a mass ratio of 1:7:3. The

Fig. 1. Schematic preparation of Co@N/C-Joule, Co@N/C-Tube, and CoO/N/C-Joule catalysts synthesized by pyrolysis of ZIF-67.

cathode catalyst slurry was coated onto to a piece of hydrophobic carbon cloth and dried, while the $Co(OH)_2$-PPy-BP slurry was coated onto a piece of Ni foam and dried. Nafion N117 and N212 membranes were used as the electrolyte. The membrane electrode assembly was pressed together by the mechanical force of the end plates without hot pressing. The fuel consisted of an alkaline solution containing 5 wt% $NaBH_4$, 10 wt% NaOH and 85 wt% deionized water, supplied at a flow rate of 50 mL min^{-1} by a peristaltic pump. Humidified O_2 was supplied to the cathode at a flow rate of 100 mL min^{-1} and a pressure of 0.25 MPa. During durability tests, the fuel was replaced roughly every 12 h.

The electrochemical impedance spectroscopy (EIS) measurements were performed using an InterFace 1000 (Gamry) instrument with a frequency range from 100 kHz to 0.01 Hz. The applied bias voltage was 5 mV.

3. Results and discussion

The prepared ZIF-67 exhibits a dodecahedral morphology with particle sizes range of 300–400 nm. (Fig. S2). The precursors were pyrolyzed at a temperature of 760 °C, with a ramp rate of up to 2429 °C s^{-1} and a cooling rate of 159 °C s^{-1} (Fig. S3). Fig. 2a exhibits the X-ray diffractometer (XRD) patterns of the prepared catalysts, and the standard XRD cards of C (JCPDS#75-2078), Co (JCPDS#15-0806) and CoO (JCPDS#71-1178) are also provided. It reveals that both Co@N/C-Joule and Co@N/C-Tube nanocatalysts prepared under argon atmosphere exhibit three diffraction peaks at 44°, 51°, and 75°, corresponding to the

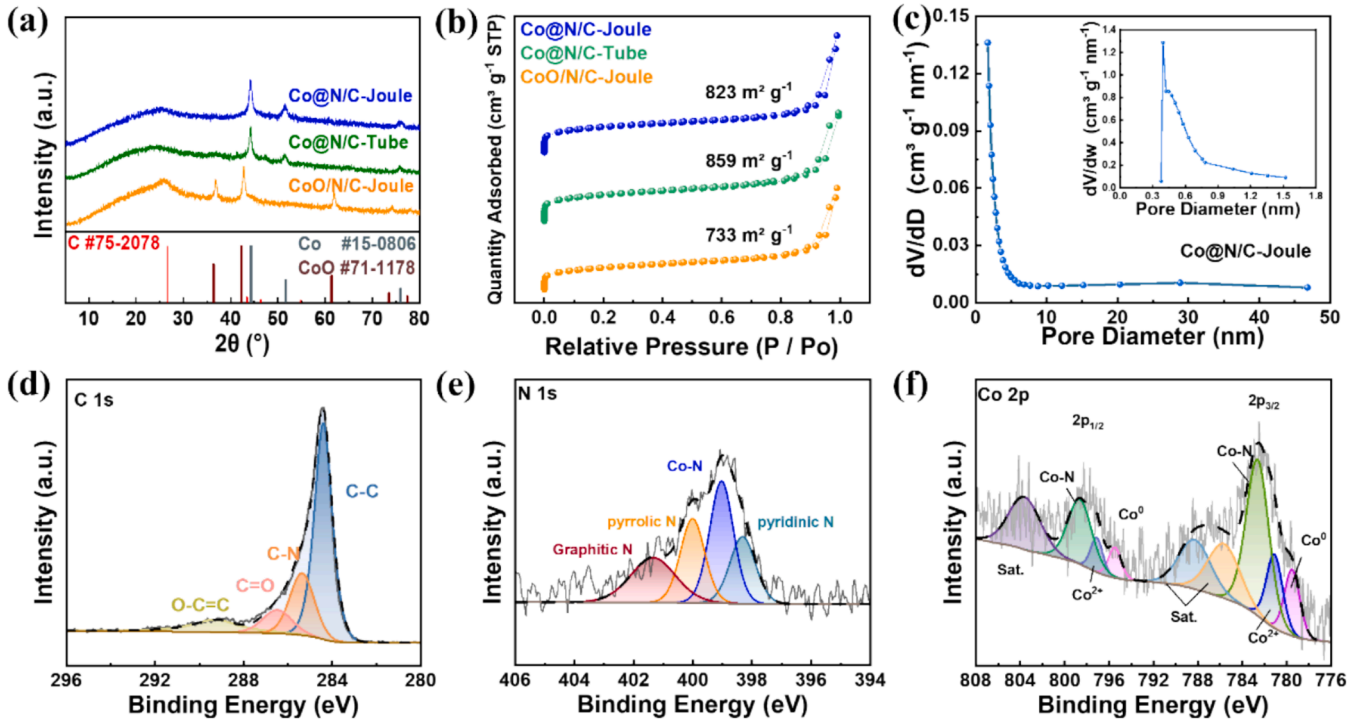

Fig. 2. (a) The XRD patterns ; (b) N_2 sorption isotherm profile of Co@N/C-Joule, Co@N/C-Tube, and CoO/N/C-Joule catalysts; (c) the pore size distribution curve of Co@N/C-Joule; XPS spectra of (d) C1s, (e) N1s, and (f) Co 2p for Co@N/C-Joule.

(111), (200), and (220) planes of metallic Co. In contrast, the CoO/N/C-Joule catalyst prepared under air atmosphere exhibits five diffraction peaks at 36°, 42°, 61°, 73°, and 77°, corresponding to the (111), (200), (220), (311), and (222) planes of CoO. The crystallite size of all samples was calculated from Fig. 2a by the Scherrer equation and compared in the Table S1. The average crystallite size of Co@N/C-Joule, CoO/N/C-Joule and Co@N/C-Tube is 11.2 nm, 9.7 nm and 15.4 nm. The diffraction peak observed at 26° in the XRD patterns of Co@N/C-Joule, CoO/N/C-Joule, and Co@N/C-Tube corresponds to the (002) plane of the BP2000 carbon support. The carbon diffraction peak in CoO/N/C-Joule is sharper than that of Co@N/C-Joule, suggesting a higher degree of graphitization when BP2000 is pyrolyzed in air compared to an Ar atmosphere.

The Brunauer Emmett Teller (BET) surface areas and pore sizes of the Co@N/C-Joule, CoO/N/C-Joule, Co@N/C-Tube and Pt/C were carried out using the N_2 absorption isotherms and the BET results are given in Fig. 2(b, c), S4, S5 and Table S2. The N_2 sorption isotherms of Co@N/C-Joule, CoO/N/C-Joule, Co@N/C-Tube, and commercial Pt/C were similar to the IV-type isotherms with an adsorption–desorption hysteresis loop in the P/P_0 range of 0.8 ~ 1, implying the micro/ mesoporous structures of the Co@N/C-Joule, CoO/N/C-Joule, Co@N/C-Tube, and Pt/C sample. The profile of Co@N/C-Joule has a bigger hysteresis loop than that of CoO/N/C-Joule in the region $0.8 < P/P_0 < 1.0$, suggesting enhanced mesopores in Co@N/C-Joule (Fig. 2b).This observation is further corroborated by the analysis of pore size distribution (Fig. 2c, Fig. S5 and Table S2), which revealed that Co@N/C-Joule possesses a micropore area of 282.5 $cm^2\ g^{-1}$ and a mesopore area of 306.5 $cm^2\ g^{-1}$. These values are higher than those observed for CoO/N/C-Joule (micropore area: 234.0 $cm^2\ g^{-1}$, mesopore area: 302.3 $cm^2\ g^{-1}$) and Pt/C (micropore area: 47.2 $cm^2\ g^{-1}$, mesopore area: 81.4 $cm^2\ g^{-1}$). With the increase of micropores, the BET specific surface area of Co@N/C-Joule slightly increased from 733 $m^2\ g^{-1}$ for CoO/N/C-Joule to 823 $m^2\ g^{-1}$. Furthermore, the Co@N/C-Tube also exhibited high BET specific surface area (859 $cm^2\ g^{-1}$) and micropore area (507.5 $cm^2\ g^{-1}$). Therefore, the core-shell structure of Co@N/C-Joule and Co@N/C-Tube is helpful to form micropores in the catalyst, which might benefit mass transport in the electrochemical processes of ORR.

The corresponding high-resolution X-ray photoelectron spectroscopy (XPS) C1s spectrum of Co@N/C-Joule Co@N/ C-Tube, and CoO/N/C-Joule nanocatalysts were deconvoluted into C-C (284.4 eV), C-N (285.4 eV), O-C = O (289.3 eV), and C = O (286.5 eV) (Hsieh et al., 2024; Khodabakhshi et al., 2024; Li et al., 2023) (Fig. 2d, Fig. S6a, d). As shown in Fig. 2e, the high-resolution N 1 s spectrum could be fitted to pyridine nitrogen (398.3 eV), Co-N_x (399.0 eV), pyrrole nitrogen (399.9 eV), and graphitic nitrogen (401.4 eV) (Akula et al., 2023; Lu et al., 2018). A comparison of the N1s XPS spectra for the Co@N/C-Joule, Co@N/ C-Tube, and CoO/N/C-Joule nanocatalysts reveals that the Co@N/C-Joule exhibits a higher content of pyridine-N, Co-N and graphite-N, which account for 76.1 % of the total nitrogen content (Fig. 2e, Fig. S6b, e, and Table S3). In contrast, the corresponding values for Co@N/C-Tube and CoO/N/C-Joule are 70.5 % and 68 %, respectively. These nitrogen species, particularly pyridinic-N, Co-N, and graphitic-N, are widely recognized as active sites that play crucial roles in facilitating the ORR (Akula et al., 2023). For instance, pyridinic nitrogen is known to optimize the adsorption of oxygen species, effectively reducing the energy barrier for the formation of reaction intermediates and facilitating a four-electron transfer pathway (Ha et al., 2020). The improvement in ORR activity observed for the Co@N/C-Joule catalyst may be attributed to the higher relative content of these beneficial nitrogen species, consistent with previous findings (Liu et al., 2023; Pan et al., 2024; Xuan et al., 2021). The Co 2p spectrum of Co@N/C-Joule is deconvoluted into Co^0 (779.5 eV and 795.8 eV), Co-N (782.6 eV and 798.5 eV) and Co^{2+} (781.1 eV and 797.0 eV), which indicating the existence of metallic cobalt, Co^{2+} and Co-N (Fig. 2f) (Akula et al., 2023; Huang et al., 2019; Mao et al., 2022). The Co 2p spectrum of Co@N/C-Tube nanocatalysts shown in Fig. S6c, exhibit characteristic peaks similar to Co@N/C-Joule nanocatalyst. Additionally, the Co 2p spectrum of CoO/N/C-Joule nanocatalyst presented in Fig. S6f reveals that the Co 2p peak consists of two distinct peaks of Co^{2+}(780.7 eV and 796.6 eV). This confirms that the Co species in CoO/N/C-Joule exists predominantly as Co^{2+}, in accordance with the XRD results. Furthermore, Table S4 presents the elemental compositions of the Co@N/C-Joule, CoO/N/C-Joule, and Co@N/C-Tube catalysts as determined by XPS analysis. The Co@N/C-Joule and CoO/N/C-Joule catalysts exhibited higher atomic fractions of Co and N compared to Co@N/C-Tube. This suggests that the rapid heating and cooling rates associated with the CTS process may promote the retention of Co and N within the catalyst structure.

The transmission electron microscope (TEM) and high resolution transmission electron microscope (HRTEM) images of the Co@N/C-Joule catalyst reveal the formed Co NPs had an average size of 11 nm and were intensively distributed on the surface of the carbon (Fig. 3a, d and Fig. S7b), with diffraction rings matching the (111), (200), and (220) crystal planes, confirming the presence of Co. HRTEM image reveals lattice fringes with a spacing of 0.203 nm, consistent with Co (1 1 1) planes, and a 1–2 nm carbon shell with 0.34 nm spacing, matching graphite, as shown in Fig. 3d. It indicates that after CTS of ZIF-67 and carbon powder under an argon atmosphere, a core–shell structure with a carbon-encapsulated cobalt core is formed. In contrast, the CoO/N/C-Joule catalyst (Fig. 3b, e and Fig. S7a) displays 8 nm CoO nanoparticles without a carbon shell. The lattice spacing of CoO nanoparticles is 0.240 nm, corresponding to the CoO (1 1 1) plane. As for the ZIF-67 derivatives prepared by tube furnace heating (Fig. 3c, f), its original three-dimensional morphology completely collapsed, and the Co@N/C-Tube derived Co NPs coarsened into larger NPs with average sizes of 18 nm, with pronounced lattice fringes (0.207 nm), and a 2-3 nm graphitic carbon shell (Fig. S7c).

Fig. 3g–i presents a high-angle annular dark field scanning transmission electron microscopy (HAADF-STEM) image and energy-dispersive X-ray spectroscopy (EDX) elemental mapping of the Co@N/C-Joule, CoO/N/C-Joule, and Co@N/C-Tube nanocatalysts. It was observed that the derived Co NPs were encapsulated in a carbon matrix, which facilitates the stabilization of cobalt nanoparticles through interfacial bonding or physical anchoring (Irmawati et al., 2023). Thus, Co@N/C-Joule and Co@N/C-Tube catalysts prepared under argon atmosphere consist of Co nanoparticles with graphitic carbon shells. In contrast, CoO/N/C-Joule catalysts prepared in air atmosphere contain smaller CoO nanoparticles without carbon shells. Prolonged pyrolysis in a tube furnace results in larger particles, while rapid heating/cooling in the carbothermal process produces smaller nanoparticles and thinner carbon shell. This is attributed to the rapid CTS process, characterized by a heating rate of 2429 °C s^{-1}, induces the instantaneous decomposition of metal precursors and ligands. This decomposition generates a large volume of rapidly diffusing gases that act as pore-forming agents, resulting in the formation of porous structures with thin, two-dimensional carbon sheets, rather than dense and compact structures (Shi et al., 2023).

X-ray absorption fine structure (XAFS) tests were conducted to investigate the atomic coordination environments of the Co@N/C-Joule, CoO/N/C-Joule, and Co@N/C-Tube nanocatalysts. The X-ray near-edge absorption (XANEs) spectra of the Co@N/C-Joule, CoO/N/C-Joule and Co@N/C-Tube, along with standard CoO and Co foil sample for reference (Fig. 4a). The Co *K*-edge spectra of both the Co@N/C-Joule and Co@N/C-Tube nanocatalysts are closely similar to those of the Co foil reference without obvious edge front peak and sharp white edge peak. This spectral similarity indicates the presence of predominantly Co in the 0 valent state within Co@N/C-Joule and Co@N/C-Tube. In contrast, the Co *K*-edge spectra of the CoO/N/C-Joule nanocatalysts, sintered in air atmosphere, is closely similar to that of the CoO reference, indicating the predominant presence of Co in the + 2 valent state.

Additionally, the extended X-ray absorption fine structure (EXAFS) data in Fig. 4b confirms that the peak positions in the *R*-space of the

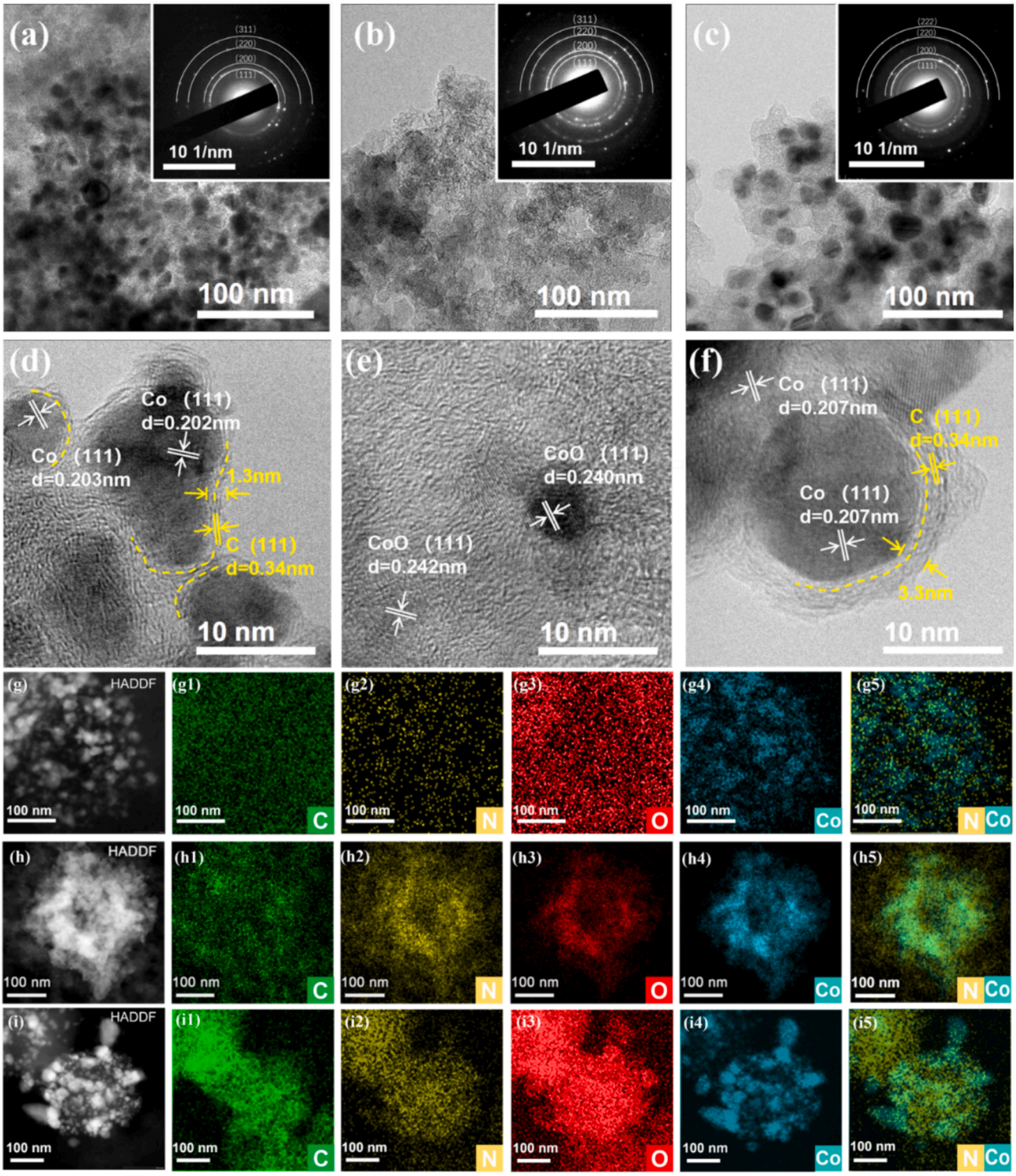

Fig. 3. TEM and HRTEM images of (a, d) Co@N/C-Joule, (b, e) CoO/N/C-Joule, and (c, f) Co@N/C-Tube, respectively; (g) HAADF-STEM and (g1-g5) STEM-EDX of Co@N/C-Joule; (h) HAADF-STEM and (h1-h5) STEM-EDX images of CoO/N/C-Joule catalysts; (i) HAADF-STEM and (i1-i5) STEM-EDX images of Co@N/C-Tube.

Co@N/C-Joule and Co@N/C-Tube nanocatalysts correspond to those of the Co foil. These confirm that the derived Co prepared under argon atmosphere, predominantly in the 0-valent Co state. Furthermore, we conducted fitting analysis on the Co@N/C-Joule catalyst, with the fitting plot shown in Fig. 4c and the fitting parameters detailed in Table S5. The *R*-space data of the Co@N/C-Joule nanocatalyst displays a peak position of Co at 2.49 Å, which indicates Co-Co coordination. Interestingly, compared to the standard Co foil, the Co@N/C-Joule nanocatalyst predominantly exhibits Co-Co coordination as its primary coordination mode, accompanied by a minor presence of Co-N coordination. This is attributed to the formation of Co-N bonds in Co@N/C effectively substitutes some of the Co-Co bonds that would be present in pure Co metal, thus decreasing the Co-Co coordination number. So the coordination number of Co-Co in the Co@N/C-Joule catalyst was fitted

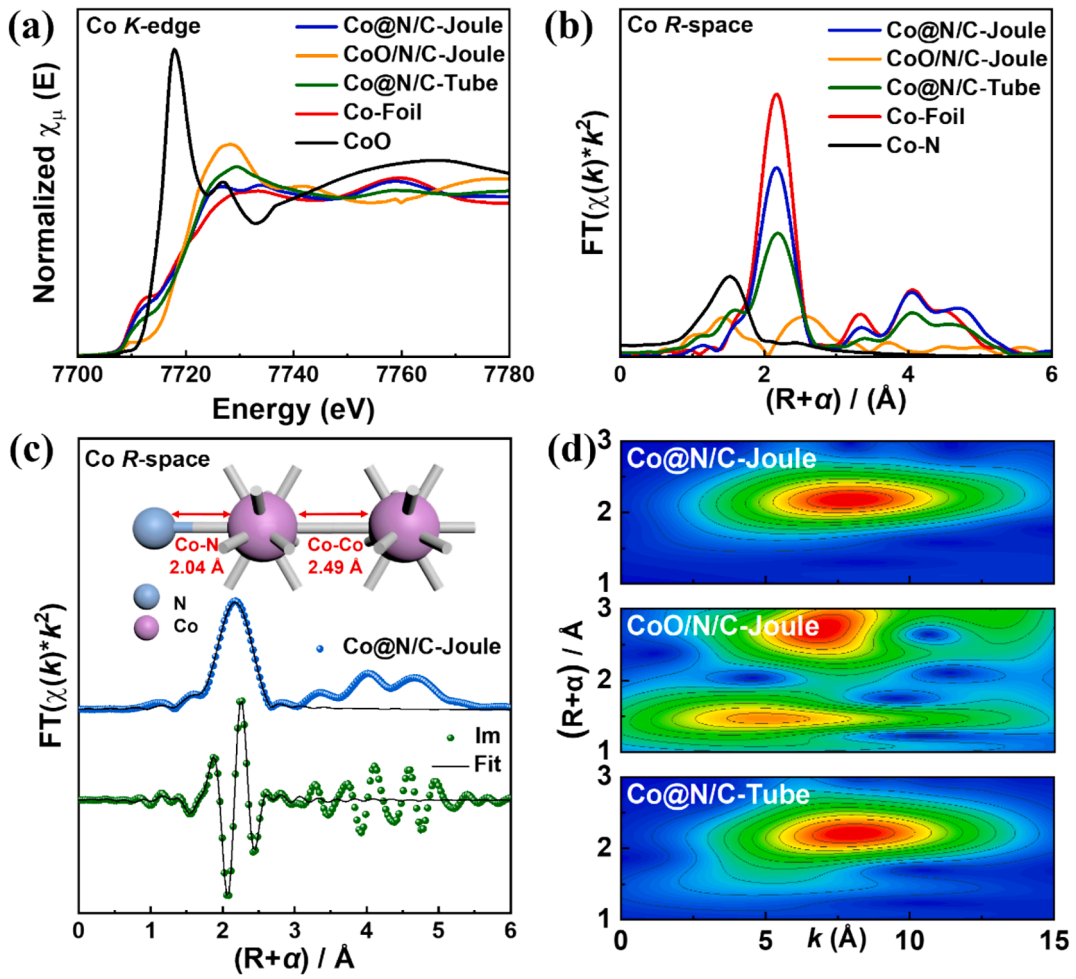

Fig. 4. (a) The Co *K*-edge XANES of Co@N/C-Joule, CoO/N/C-Joule, Co@N/C-Tube, CoO and Co foil; (b) The Fourier transform (FT) of the Co *K*-edge EXAFS of Co@N/C-Joule, CoO/N/C-Joule, Co@N/C-Tube, and Co foil at *R*-space, *k*-weight set to 2; (c)The fitting of Co@N/C-Joule, and inset is the fitted structure at *R*-space, *k*-weight set to 2; (d) The wavelet transformed plots for the K^3-weight EXAFS signals of the Co@N/C-Joule, CoO/N/C-Joule, and Co@N/C-Tube.

to be 11.0 (± 0.5), which was lower than the 12 in Co foil. The coordination number of Co-N in the Co@N/C-Joule catalyst was fitted to be 1.75 (± 0.1), suggesting that the Co-N coordination in Co@N/C-Joule exists in the form of CoN_2. Co-N and Co nanoparticles are commonly regarded as one of the active sites for oxygen reduction reaction. Therefore, the high content of Co-N and Co nanoparticles in the Co@N/C-Joule nanocatalysts can enhance the ORR activity. In conjunction with HRTEM data, indicates that the Co@N/C-Joule nanocatalyst comprises Co nanoparticles and Co-N at the interface between the graphite carbon shell and the Co core particles (Liu et al., 2022; Sun et al., 2023; Zhao et al., 2022). This structure is visually represented in the localized fine-structure maps of Co atoms as shown in Fig. 4c. For the direct observation of the structural characteristics of *K*-space and *R-space* (Funke et al., 2005), the wavelet transform (WT) data of the K^3-weighted EXAFS spectrum is presented in Fig. 4d. A single intensity maximum near 8 Å was found in the Co@N/C-Joule nanocatalyst. Comparison with the WT of the reference Co foil (Fig. S8) reveals a similar intensity maximum at the same location in *K*-space. This consistent localization of the single intensity maximum suggests that it arises from the first-shell Co-Co scattering path in both Co@N/C catalysts, indicating the presence of Co-Co coordination. It further supports the notion that the Co species in the catalyst primarily exist as Co nanoparticles in Co@N/C-Joule (Ha et al., 2020). In contrast, the CoO/N/C-Joule nanocatalysts display two intensity maxima near 7–8 Å, representing the scattering paths of Co-Co and Co-O, respectively. The WT analysis of the Co@N/C-Tube exhibits a similar pattern to that of the Co foil, with an intensity maximum near 8 Å corresponding to the scattering path of the Co-Co first shell layer. The TEM results combined with these findings confirm that the Co@N/C-Joule and Co@N/C-Tube, prepared through sintering under an Ar atmosphere, consist of Co nanoparticles encapsulated by nitrogen doped carbon shell.

Fig. 5a shows the cyclic voltammetry (CV) curves of Co@N/C-Joule, CoO/N/C-Joule, Co@N/C-Tube nanocatalysts, and Pt/C catalyst. The CV curves of the four catalysts show obvious peaks only under an O_2-saturated electrolyte rather than Ar. In addition, the reduction peaks of Co@N/C-Joule, CoO/N/C-Joule, and Co@N/C-Tube nanocatalysts respectively exhibited onset reduction potentials (E_{onset}) of 0.92 V, 0.89 V, and 0.93 V. Fig. 5b illustrates the linear sweep voltammetry (LSV) of Co@N/C-Joule, CoO/N/C-Joule, Co@N/C-Tube, and Pt/C measured at 1600 rpm, and the RDE curves at different rotational speeds are shown in Fig. S9. The Co@N/C-Joule, CoO/N/C-Joule, and Co@N/C-Tube nanocatalysts exhibited $E_{1/2}$ of 0.84 V, 0.835 V, and 0.83 V, respectively, which are close to the $E_{1/2}$ of the Pt/C (0.86 V), as shown in Fig. 5c. The number of transferred electrons (*n*) for Co@N/C-Joule, CoO/N/C-Joule, Co@N/C-Tube, and Pt/C were calculated using the Koutecký-Levich equation and were determined to be 4.12, 3.63, and 3.73, respectively (Fig. S10a–c). Fig. 5d presents the number of transferred electrons and the H_2O_2 yields of Co@N/C-Joule, CoO/N/C-Joule, Co@N/C-Tube nanocatalysts, and Pt/C measured by RRDE technique. All of the number of transferred electrons exceed 3.5, while the H_2O_2 yields remain below 10 %. This provides further confirmation that these catalysts catalyze the ORR *via* a four-electron transfer pathway (Liu

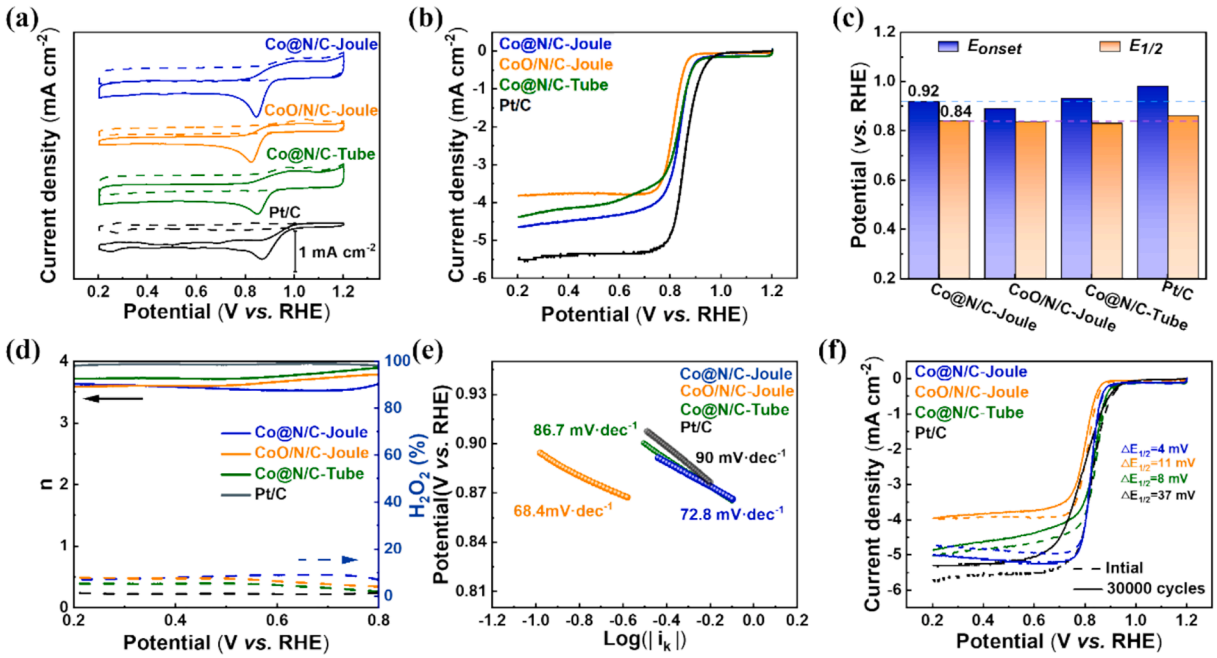

Fig. 5. The electrocatalytic performances of Co@N/C-Joule, CoO/N/C-Joule, Co@N/C-Tube nanocatalysts, and commercial Pt/C toward the ORR in a 0.1 M KOH solution. (a) CV curves obtained at 10 mV/s under O_2 (solid line) and Ar (dashed line) saturation; (b) LSV curves measured at 10 mV/s and at 1600 rpm; (c) The comparison of the initial reduction potential and half-wave potential; (d) Plot of the number of transferred electrons (n) and H_2O_2 yields; (e) Tafel slopes plots at 1600 rpm; (f) The ORR-LSV curves before and after 30,000 cycles.

et al., 2022; Song et al., 2021).

As shown in Fig. 5e, the Tafel slopes of Co@N/C-Joule, CoO/N/C-Joule, and Co@N/C-Tube nanocatalysts are 72.8, 68.4, and 86.7 mV dec^{-1}, respectively, which is lower than commercial Pt/C catalyst (90 mV dec^{-1}). These indicate that non-precious metal catalysts, including Co@N/C-Joule, CoO/N/C-Joule, and Co@N/C-Tube demonstrate superior reaction kinetics compared to the commercial Pt/C catalyst. The electrochemical active surface areas (ECSAs) of the three nanocatalysts

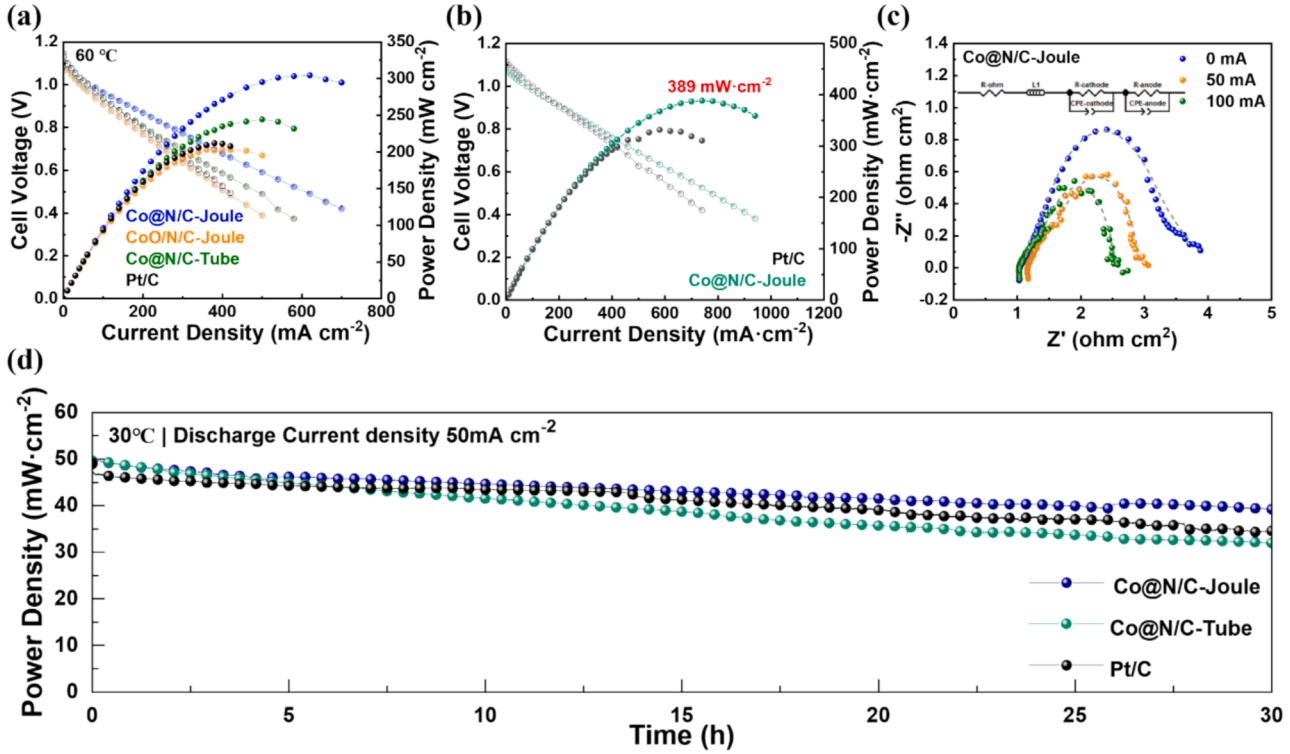

Fig. 6. (a) *I-V* curves of DBFC using Co@N/C-Joule, CoO/N/C-Joule, Co@N/C-Tube, and Pt/C cathode operated at 60 °C, the electrolyte membrane is N117. (b) *I-V* curves of DBFC using Co@N/C-Joule and Pt/C cathode operated at 60 °C, the electrolyte membrane is N212. (c) The Nyquist plots of the DBFC using Co@N/C-Joule cathode at 30 °C, with an inset showing the corresponding equivalent circuit diagrams (d) The durability test of DBFCs using Co@N/C-Joule, Co@N/C-Tube, and Pt/C cathode operated at 30 °C, with a discharge current density of 50 mA cm^{-2}.

and the commercial Pt/C catalyst were calculated within the non-Faradaic potential region at different scan rates (10–80 mV s^{-1}) using CV curves, as shown in Fig. S11. The calculated ECSA values for Co@N/C-Joule, CoO/N/C-Joule, and Co@N/C-Tube nanocatalysts are 49.3 cm^2, 24.0 cm^2, and 71.6 cm^2, respectively, which are 4.7, 2.3, and 6.8 times greater than the ECSA of the Pt/C commercial catalyst (10.5 cm^2). The accelerated deterioration tests (ADT) tests were performed on all samples to assess the durability in an alkaline environment (Fig. 5f). After 30,000 cyclic voltammetry cycles, the $E_{1/2}$ of the Co@N/C-Joule, CoO/N/C-Joule, and Co@N/C-Tube nanocatalysts exhibited negatively shifts of 4 mV, 11 mV, and 8 mV, respectively, in contrast to the Pt/C catalyst that experienced a 37 mV shift under identical testing conditions. Furthermore, the comparison between the before and after 30,000 CV cycling curves reveals an increase in the limiting current density of LSV for Co@N/C-Joule, indicating an enhancement of its electrocatalytic activity towards ORR after the ADT test. Comparison of the $E_{1/2}$ after durability testing of Co@N/C-Joule catalysts with non-precious metal catalysts that have been reported in the literature also reveals that Co@N/C-Joule catalysts have better durability performance (Table S6). The Co@N/C-Joule and Co@N/C-Tube nanocatalyst exhibit excellent durability, which can be attributed to the formation of core-shell structure comprising carbon-coated cobalt nanoparticles (Jin et al., 2023; Xi et al., 2024).

The cell performance of DBFCs using the Co@N/C-Joule, CoO/N/C-Joule, Co@N/C-Tube nanocatalysts, or the Pt/C cathode are presented in Fig. 6a, S12 and Table S7. At 30 °C, the open circuit voltages of Co@N/C-Joule, CoO/N/C-Joule, and Co@N/C-Tube nanocatalysts all exceeded 1.10 V, and the maximum power densities of the Co@N/C-Joule (125 mW cm^{-2}), CoO/N/C-Joule (129 mW cm^{-2}), and Co@N/C-Tube (131 mW cm^{-2}) were surpassed that of the Pt/C catalyst (106 mW cm^{-2}) (Fig. S12). At 60 °C, the CoO/N/C-Joule and Co@N/C-Tube nanocatalysts achieved maximum power densities of 203 mW cm^{-2} and 245 mW cm^{-2}, respectively. Notably, the Co@N/C-Joule nanocatalyst exhibits a remarkable maximum power density of 304 mW cm^{-2}, which surpasses that of DBFC using Pt/C cathode (212 mW cm^{-2}). When using N212 membrane, the DBFC assembled with the Co@N/C-Joule nanocatalyst achieved a maximum power density of 389 mW cm^{-2}, which surpasses that of DBFC using Pt/C cathode (332 mW cm^{-2}) (Fig. 6b). Comparison of maximum power density of the DBFC using Co@N/C-Joule cathode with the DBFC using Me/N/C catalysts that have been reported in the literature also reveals that the DBFC using Co@N/C-Joule cathode has better cell performance (Table S8).

The EIS tests were conducted to investigate the factors contributing to the variations in cell performance among the three nanocatalysts. Fig. 6c and Fig. S13 (a, b) present the EIS analysis results for Co@N/C-Joule, CoO/N/C-Joule, and Co@N/C-Tube nanocatalysts under open-circuit conditions and discharge currents of 50 mA and 100 mA at 30 °C, respectively. Previous studies on porous electrodes for fuel cells have indicated that the high-frequency semicircle reflects the ohmic resistance in fuel cell electrolyte, while the low-frequency semicircle reflects the electrochemical reaction of the catalyst on the electrode (Lin et al., 2019). Equivalent circuit fitting was performed on the EIS results, as shown in Table S9. The cathode impedances of Co@N/C-Joule nanocatalyst was 1.72 Ω) during open circuit and 0.811 Ω under a discharge current of 100 mA. In comparison, the cathode impedances of Co@N/C-Tube nanocatalyst demonstrated high values of 2.74 Ω during open circuit and 1.479 Ω under a discharge current of 100 mA, while the cathode impedances of CoO/N/C-Joule nanocatalyst exhibited 1.69 Ω during open circuit and 1.226 Ω under a discharge current of 100 mA. These findings suggest that the smaller particle size of the catalyst and the thinner carbon shell coating, which contribute to lower resistance, enhanced conductivity, and improved power generation performance of the single cell in both open-circuit and discharge states. To further explore the stability of the DBFCs using Co@N/C-Joule and Co@N/C-Tube cathode, the DBFCs was discharged at 50 mA cm^{-2} at 30 °C, and the results were shown in Fig. 6d. After 30 h of discharge, the power density of Co@N/C-Joule remains at 39 mW cm^{-2}, which is better than Co@N/C-Tube catalyst (32 mW cm^{-2}) and Pt/C (35 mW cm^{-2}). This observation suggests that the Co@N/C-Joule cathode catalyst exhibits good stability.

The HRTEM image of the Co@N/C-Joule catalyst after stability test shows the Co NPs with an averaged particle size of 10 nm dispersed on the carbon surface, with diffraction rings matching the (111), (200), and (220) crystal planes, confirming the presence of Co (Fig. 7). The Co nanoparticles were encapsulated by carbon shell. The XRD patterns of the Co@N/C-Joule and Co@N/C-Tube catalyst after stability test are shown in Fig. S14. It indicates that after the durability test, the physical phase and a core-shell structure of Co@N/C-Joule catalyst are kept, confirming the effective protective role of the graphitic carbon shells in preserving the structure of the Co@N/C-Joule and highlighting the significance in enhancing catalyst stability.

Accordingly, the electrocatalytic reaction mechanism of Co@N/C nanocatalysts with a core-shell structure for ORR was proposed and shown in Fig. 8. The highly efficient catalytic activity and durability of Co@N/C nanocatalysts for towards ORR can be attributed to two factors. Firstly, the core-shell structure, comprising Co nanoparticles embedded within the nitrogen-doped graphitic carbon layer, act as the electrocatalytically active sites for ORR. The strong bonding between Co particles and graphitic carbon shells facilitates the adsorption and activation of oxygen molecules, enhancing the catalytic activity (Xie et al., 2021). Since Co-N_x sites and metallic cobalt nanoparticles are commonly regarded as active sites for the ORR, the high density of these species in the Co@N/C-Joule nanocatalysts could contribute to the enhanced ORR activity. Therefore, the rapid heating and cooling rate of CTS enables the production of small-sized Co@N/C nanocatalysts, thereby increasing the surface density of active sites on Co nanoparticles and Co-N sites, which leads to improved ORR performance (Shi et al., 2023). The enhanced catalytic stability is also attributed to the core-shell structure encapsulated by an appropriately thickness carbon shell. The carbon shell thickness of Co@N/C nanocatalysts synthesized through the CTS of ZIF-67 is thinner than that of Co@N/C nanocatalysts prepared using a tubular furnace pyrolysis method. This thinner carbon shell not only effectively preserves the structural stability of the cobalt particles but also enhances the catalyst's electrical conductivity, thereby achieving superior catalytic performance (Cho, 2008; Li et al., 2017). Therefore, the core-shell structure of Co@N/C-Joule could offer unique opportunities to leverage surface properties and interfacial interactions for enhanced electrocatalytic activity in the ORR. The Co core influences the overall electronic properties of the Co@N/C-Joule, while the carbon shell, in direct contact with the reactants, plays a critical role in the electrocatalytic process. The interface between the Co core and carbon shell can further induce electronic and geometric effects that synergistically optimize adsorption energies and promote favorable reaction pathways for enhanced ORR activity. The Co@N/C nanocatalyst prepared through the CTS pyrolysis of ZIF-67 under an argon atmosphere represents an efficient approach for synthesizing non-precious metal cathode catalysts for fuel cells.

4. Conclusions

In conclusion, this paper presents the synthesis of Co@N/C nanocatalysts with a core-shell structure through the carbothermal pyrolysis of ZIF-67 in an argon atmosphere. This preparation method effectively combines the advantages of inert atmosphere and carbothermal shock method, producing stable non-precious metal catalysts with low energy consumption and high efficiency. Moreover, the Co@N/C-Joule nanocatalysts demonstrated excellent performance as cathode catalysts in DBFC, showing promising cell performance and stability. The superior catalytic performance is attributed to the catalysts' small nanoparticle size and the thin nitrogen-doped carbon shell. These results provide valuable insights for optimizing non-precious metal cathode catalysts in DBFC.

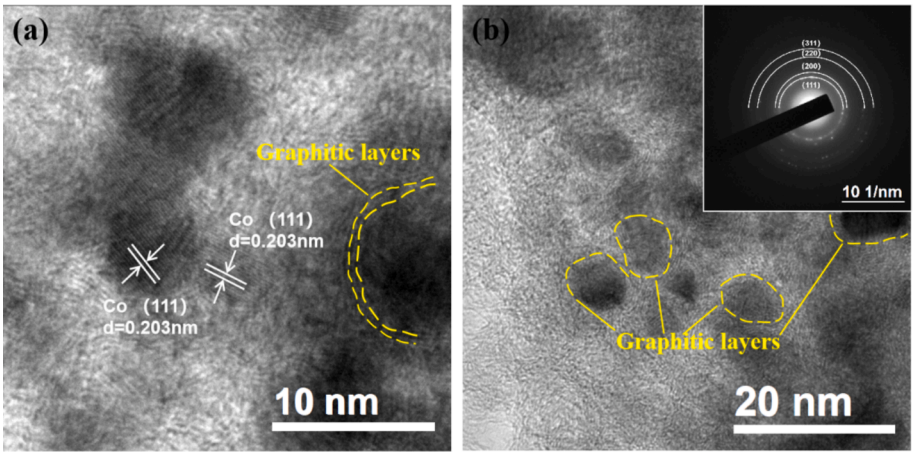

Fig. 7. (a, b) The HRTEM images of Co@N/C-Joule nanocatalysts after the durability test of DBFC for 30 h. The inset of (b) is the corresponding diffraction rings of nanoparticles.

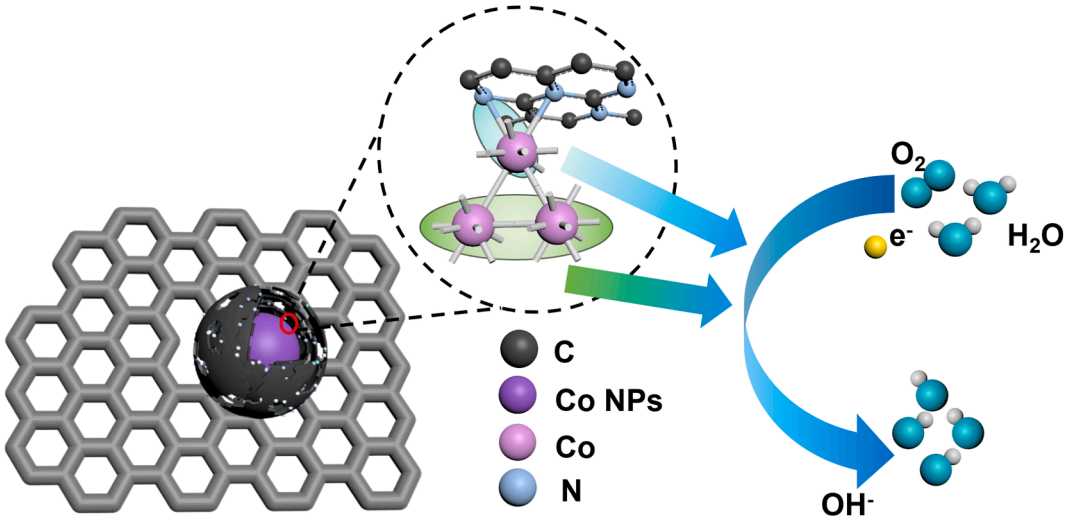

Fig. 8. The Schematic diagram of the catalytic mechanism of Co@N/C catalyst with core–shell structure.

CRediT authorship contribution statement

Lianke Zhang: Writing – review & editing, Writing – original draft, Methodology, Investigation, Formal analysis, Data curation. **Lei Zhang:** Writing – review & editing, Writing – original draft, Methodology, Investigation, Formal analysis, Data curation. **Dandan Li:** Methodology, Investigation, Data curation. **Haiying Qin:** Writing – review & editing, Supervision, Funding acquisition, Formal analysis. **Hualiang Ni:** Methodology, Investigation. **Hongzhong Chi:** Investigation, Formal analysis. **Junjing He:** Funding acquisition, Formal analysis. **Yan He:** Methodology, Investigation, Formal analysis.

Declaration of competing interest

The authors declare that they have no known competing financial interests or personal relationships that could have appeared to influence the work reported in this paper.

Acknowledgment

This work is financially supported by the Zhejiang Provincial Natural Science Foundation of China (No. LZ22B060001, LY22E010003), the "Pioneer" R&D Program of Zhejiang Province (2023C01080) and the Hangzhou Dianzi University Graduate Innovation Research Project, China (CXJJ2023172). The authors wish to thank BL11B, BL15U and the User Experiment Assist System in Shanghai Synchrotron Radiation Facilities, China (SSRF).

Appendix A. Supplementary data

Supplementary data to this article can be found online at https://doi.org/10.1016/j.ces.2024.120953.

Data availability

Data will be made available on request.

References

Akula, S., Mooste, M., Kozlova, J., Käärik, M., Treshchalov, A., Kikas, A., Kisand, V., Aruväli, J., Paiste, P., Tamm, A., Leis, J., Tammeveski, K., 2023. Transition metal (Fe Co, Mn, Cu) containing nitrogen-doped porous carbon as efficient oxygen reduction electrocatalysts for anion exchange membrane fuel cells. Chem. Eng. J. 458, 141468.

Cho, J., 2008. Control of the carbon shell thickness in $Sn_{70}Ge_{30}$@carbon core-shell nanoparticles using alkyl terminators: Its implication for high-capacity lithium battery anode materials. Electrochim. Acta 54, 461–466.

Chung, H.T., Won, J.H., Zelenay, P., 2013. Active and stable carbon nanotube/nanoparticle composite electrocatalyst for oxygen reduction. Nat. Commun. 4, 1922.

Fang, Y., Ji, S.Y., Wu, X., Zhu, J.F., 2024. Lamellar structured Ce-S-NC heterogeneous electrocatalyst as the highly durable cathode for passive direct liquid fuel cells. Appl. Surf. Sci. 652, 159332–159342.
Funke, H., Scheinost, A.C., Chukalina, M., 2005. Wavelet analysis of extended x-ray absorption fine structure data. Phys. Rev. B 71, 094110.
Gao, J., Zhou, X., Wang, Y., Chen, Y., Xu, Z., Qiu, Y., Yuan, Q., Lin, X., Qiu, H.J., 2022. Exploiting the Synergistic Electronic Interaction between Pt-Skin Wrapped Intermetallic PtCo Nanoparticles and Co-N-C Support for Efficient ORR/EOR Electrocatalysis in a Direct Ethanol Fuel Cell. Small 18, e2202071.
Guo, L., Wan, X., Liu, J., Guo, X., Liu, X., Shang, J., Yu, R., Shui, J., 2024. Revealing Distance-Dependent Synergy between $MnCo_2O_4$ and Co-N-C in Boosting the Oxygen Reduction Reaction. ACS Appl. Mater. Interfaces 16, 3388–3395.
Ha, Y., Fei, B., Yan, X., Xu, H., Chen, Z., Shi, L., Fu, M., Xu, W., Wu, R., 2020. Atomically Dispersed Co-Pyridinic N-C for Superior Oxygen Reduction Reaction. Adv. Energy Mater. 10, 202002592.
Han, Y., Liu, M., Sun, L., Li, X., Yao, Y., Zhang, C., Ding, S., Liao, H., Zhang, L., Fan, F.R., Moskovits, M., Tian, Z., 2022. A general strategy for overcoming the trade-off between ultrasmall size and high loading of MOF-derived metal nanoparticles by millisecond pyrolysis. Nano Energy 97, 107125.
Han, M., Shi, M., Wang, J., Zhang, M., Yan, C., Jiang, J., Guo, S., Sun, Z., Guo, Z., 2019. Efficient bifunctional Co/N dual-doped carbon electrocatalysts for oxygen reduction and evolution reaction. Carbon 153, 575–584.
Hsieh, T., Chang, T., Lin, Y., Lin, J., 2024. One-step generation of hollow graphitic carbon nanospheres with suitable oxygenated structures as conductive additives for water-soluble binder in highly stable supercapacitor electrodes. Electrochim. Acta 483, 144050.
Huang, K., Zhang, W., Li, J., Fan, Y., Yang, B., Rong, C., Qi, J., Chen, W., Yang, J., 2019. In Situ Anchoring of Zeolite Imidazole Framework-Derived Co, N-Doped Porous Carbon on Multiwalled Carbon Nanotubes toward Efficient Electrocatalytic Oxygen Reduction. ACS Sustainable Chem. Eng. 8, 478–485.
Irmawati, Y., Balqis, F., Destyorini, F., Adios, C.G., Yudianti, R., Iskandar, F., Sumboja, A., 2023. Cobalt Nanoparticles Encapsulated with N-Doped Bamboo-Like Carbon Nanofibers as Bifunctional Catalysts for Oxygen Reduction/Evolution Reactions in a Wide pH Range. ACS Appl. Nano Mater. 6, 2708–2718.
Jin, L., Chen, J., Fu, Z., Qian, X., Cheng, J., Hao, Q., Zhang, K., 2023. ZIF-8/ZIF-67 derived ZnS@Co-N-C hollow core-shell composite and its application in lithium-sulfur battery. Sustainable Mater. Technol. 35, e00571.
Khodabakhshi, S., Fulvio, P.F., Walton, K.S., Kiani, S., Niu, Y., Palmer, R.E., Barron, A.R., Andreoli, E., 2024. High surface area microporous carbon nanocubes from controlled processing of graphene oxide nanoribbons. Carbon 221, 118940.
Kim, C., Dionigi, F., Beermann, V., Wang, X., Moller, T., Strasser, P., 2019. Alloy Nanocatalysts for the Electrochemical Oxygen Reduction (ORR) and the Direct Electrochemical Carbon Dioxide Reduction Reaction (CO_2RR). Adv. Mater. 31, e1805617.
Kuang, L., Zhang, L., Lü, S., Wei, J., Zhou, Y., Qin, H., He, J., Zhang, Z., Ni, H., He, Y., 2024. Atomically dispersed high-loading Pt-Fe/C metal-atom foam catalyst for oxygen reduction in fuel cells. J. Alloys Compd. 973, 172928.
Kumar, R., Mooste, M., Ahmed, Z., Akula, S., Zekker, I., Marandi, M., Käärik, M., Leis, J., Kikas, A., Treshchalov, A., Otsus, M., Aruväli, J., Kisand, V., Tamm, A., Tammeveski, K., 2023. Highly active ZIF-8@CNT composite catalysts as cathode materials for anion exchange membrane fuel cells. Ind. Chem. Mater. 1, 526–541.
Li, M., Bao, C., Liu, Y., Meng, J., Liu, X., Cai, Y., Wuu, D., Zong, Y., Loh, T.P., Wang, Z., 2019. Reduced graphene oxide-supported cobalt oxide decorated N-doped graphitic carbon for efficient bifunctional oxygen electrocatalysis. RSC Adv 9, 16534–16540.
Li, J., Song, Y., Zhang, G., Liu, H., Wang, Y., Sun, S., Guo, X., 2017. Pyrolysis of Self-Assembled Iron Porphyrin on Carbon Black as Core/Shell Structured Electrocatalysts for Highly Efficient Oxygen Reduction in Both Alkaline and Acidic Medium. Adv. Funct. Mater. 27, 1604356.
Li, D., Zhang, L., Kuang, L., Qin, H., Hu, X., He, J., Ni, H., He, Y., 2023. Carbothermal shock synthesis of CoO/N/C nanoparticles with superior durability for oxygen reduction reaction. J. Power Sources 587, 233699.
Lin, Y., Song, H., Rao, H., Du, Z., Pan, Z., Zhong, X., 2019. MOF-Derived Co, N Codoped Carbon/Ti Mesh Counter Electrode for High-Efficiency Quantum Dot Sensitized Solar Cells. The Journal of Physical Chemistry Letters 10, 4974–4979.
Liu, M., Xu, Q., Miao, Q., Yang, S., Wu, P., Liu, G., He, J., Yu, C., Zeng, G., 2022. Atomic Co-N_4 and Co nanoparticles confined in COF@ZIF-67 derived core-shell carbon frameworks: bifunctional non-precious metal catalysts toward the ORR and HER. J. Mater. Chem. A 10, 228–233.
Liu, J., Xu, H., Zhu, J., Cheng, D., 2023. Understanding the Pathway Switch of the Oxygen Reduction Reaction from Single- to Double-/Triple-Atom Catalysts: A Dual Channel for Electron Acceptance-Backdonation. JACS Au 3, 3031–3044.
Lu, H., Zhang, H., Zhang, X., Sun, N., Zhu, X., Zhao, H., Wang, G., 2018. Transformation of carbon-encapsulated metallic Co into ultrafine Co/CoO nanoparticles exposed on N-doped graphitic carbon for high-performance rechargeable zinc-air battery. Appl. Surf. Sci. 448, 369–379.
Luo, H., Jiang, W.J., Niu, S., Zhang, X., Zhang, Y., Yuan, L.P., He, C., Hu, J.S., 2020. Self-Catalyzed Growth of Co-N-C Nanobrushes for Efficient Rechargeable Zn-Air Batteries. Small 16, 2001171.
Mao, J., Liu, P., Li, J., Yan, J., Ye, S., Song, W., 2022. Accelerated intermediate conversion through nickel doping into mesoporous Co-N/C nanopolyhedron for efficient ORR. J. Energy Chem. 73, 240–247.
Miao, Z., Xia, Y., Liang, J., Xie, L., Chen, S., Li, S., Wang, H.L., Hu, S., Han, J., Li, Q., 2021. Constructing Co-N-C Catalyst via a Double Crosslinking Hydrogel Strategy for Enhanced Oxygen Reduction Catalysis in Fuel Cells. Small 17, e2100735.
Pan, H., Li, Z., Ma, Q., Zhang, Y., Zheng, Y., Gao, Y., 2024. Cobalt catalyst encapsulated by N-doped carbon for selective hydrogenation of aldehyde to alcohol. Mol. Catal. 553, 113752.
Peng, H., Liu, F., Liu, X., Liao, S., You, C., Tian, X., Nan, H., Luo, F., Song, H., Fu, Z., Huang, P., 2014. Effect of Transition Metals on the Structure and Performance of the Doped Carbon Catalysts Derived From Polyaniline and Melamine for ORR Application. ACS Catal. 4, 3797–3805.
Peng, W., Yang, X., Mao, L., Jin, J., Yang, S., Zhang, J., Li, G., 2021. ZIF-67-derived Co nanoparticles anchored in N doped hollow carbon nanofibers as bifunctional oxygen electrocatalysts. Chem. Eng. J. 407, 127157.
Prieto, G., Zecevic, J., Friedrich, H., de Jong, K.P., de Jongh, P.E., 2013. Towards stable catalysts by controlling collective properties of supported metal nanoparticles. Nat. Mater. 12, 34–39.
Qin, H.Y., Liu, Z.X., Ye, L.Q., Zhu, J.K., Li, Z.P., 2009. The use of polypyrrole modified carbon-supported cobalt hydroxide as cathode and anode catalysts for the direct borohydride fuel cell. J. Power Sources 192, 385–390.
Shi, W., Li, Z., Gong, Z., Liang, Z., Liu, H., Han, Y.C., Niu, H., Song, B., Chi, X., Zhou, J., Wang, H., Xia, B.Y., Yao, Y., Tian, Z.Q., 2023. Transient and general synthesis of high-density and ultrasmall nanoparticles on two-dimensional porous carbon via coordinated carbothermal shock. Nat. Commun. 14, 2294.
Song, L., Fan, H., Wang, T., Xiang, T., Zhang, M., Hu, C., Zhou, W., He, J., 2021. Facile synthesis of Co, N enriched carbon nanotube and active site identifications for bifunctional oxygen reduction and evolution catalysis. Energy Storage Mater. 43, 365–374.
Stracensky, T., Jiao, L., Sun, Q., Liu, E., Yang, F., Zhong, S., Cullen, D.A., Myers, D.J., Kropf, A.J., Jia, Q., Mukerjee, S., Xu, H., 2023. Bypassing Formation of Oxide Intermediate via Chemical Vapor Deposition for the Synthesis of an Mn-N-C Catalyst with Improved ORR Activity. ACS Catal 13, 14782–14791.
Sun, K., Dong, J., Sun, H., Wang, X., Fang, J., Zhuang, Z., Tian, S., Sun, X., 2023. $Co(CN)_3$ catalysts with well-defined coordination structure for the oxygen reduction reaction. Nat. Catal. 6, 1164–1173.
Wang, Z., Lu, Y., Yan, Y., Larissa, T.Y.P., Zhang, X., Wuu, D., Zhang, H., Yang, Y., Wang, X., 2016. Core-shell carbon materials derived from metal-organic frameworks as an efficient oxygen bifunctional electrocatalyst. Nano Energy 30, 368–378.
Wang, A., Zhao, C., Yu, M., Wang, W., 2021. Trifunctional Co nanoparticle confined in defect-rich nitrogen-doped graphene for rechargeable Zn-air battery with a long lifetime. Appl. Catal., B 281, 119514.
Xi, W., Liu, W., Yu, A., Mu, M., Gu, W., Shi, L., 2024. Core-shell Co-NC@NC nanomaterial for efficient oxygen reduction reaction. Int. J. Hydrogen Energy 72, 141–148.
Xie, H., Liu, Y., Li, N., Li, B., Kline, D.J., Yao, Y., Zachariah, M.R., Wang, G., Su, D., Wang, C., Hu, L., 2021. High-temperature-pulse synthesis of ultrathin-graphene-coated metal nanoparticles. Nano Energy 80, 105536.
Xuan, J., Huang, N., Zhang, J., Dong, W., Yang, L., Wang, B., 2021. Fabricating Co-N-C catalysts based on ZIF-67 for oxygen reduction reaction in alkaline electrolyte. J. Solid State Chem. 294, 121788.
Yao, Y., Huang, Z., Xie, P., Lacey, S.D., Jacob, R.J., Xie, H., Chen, F., Nie, A., Pu, T., Rehwoldt, M., Yu, D., Zachariah, M.R., Wang, C., Shahbazian-Yassar, R., Li, J., Hu, L., 2018. Carbothermal shock synthesis of high-entropy-alloy nanoparticles. Science 359, 1489–1494.
Zhang, M., Dai, Q., Zheng, H., Chen, M., Dai, L., 2018. Novel MOF-Derived Co@N-C Bifunctional Catalysts for Highly Efficient Zn-Air Batteries and Water Splitting. Adv. Mater. 30, 15731.
Zhang, Y., Wang, P., Yang, J., Li, K., Long, X., Li, M., Zhang, K., Qiu, J., 2020b. Fabrication of core-shell nanohybrid derived from iron-based metal-organic framework grappled on nitrogen-doped graphene for oxygen reduction reaction. Chem. Eng. J. 401, 126001.
Zhang, C., Zhao, P., Zhang, Z., Zhang, J., Yang, P., Gao, P., Gao, J., Liu, D., 2017. Co-N-C supported on SiO_2: a facile, efficient catalyst for aerobic oxidation of amines to imines. RSC Adv. 7, 47366–47372.
Zhang, N., Zhou, T., Ge, J., Lin, Y., Du, Z., Zhong, C.A., Wang, W., Jiao, Q., Yuan, R., Tian, Y., Chu, W., Wu, C., Xie, Y., 2020a. High-Density Planar-like Fe_2N_6 Structure Catalyzes Efficient Oxygen Reduction. Matter 3, 509–521.
Zhao, Y., Kumar, P.V., Tan, X., Lu, X., Zhu, X., Jiang, J., Pan, J., Xi, S., Yang, H.Y., Ma, Z., Wan, T., Chu, D., Jiang, W., Smith, S.C., Amal, R., Han, Z., Lu, X., 2022. Modulating Pt-O-Pt atomic clusters with isolated cobalt atoms for enhanced hydrogen evolution catalysis. Nat. Commun. 13, 2430.
Zhao, J., Quan, X., Chen, S., Liu, Y., Yu, H., 2017. Cobalt Nanoparticles Encapsulated in Porous Carbons Derived from Core-Shell ZIF67@ZIF8 as Efficient Electrocatalysts for Oxygen Evolution Reaction. ACS Appl. Mater. Interfaces 9, 28685–28694.